The SARS-CoV-2 conserved macrodomain is a mono-ADP-ribosylhydrolase

Yousef M.O. Alhammad[a], Maithri M. Kashipathy[b], Anuradha Roy[c], Jean-Philippe Gagné[d,e], Peter McDonald[c], Philip Gao[f], Louis Nonfoux[d,e], Kevin P. Battaile[g], David K. Johnson[h], Erik D. Holmstrom[a], Guy G. Poirier[d,e], Scott Lovell[b] and Anthony R. Fehr[a,#]

[a]Department of Molecular Biosciences, University of Kansas, Lawrence, Kansas 66045, USA
[b]Protein Structure Laboratory, University of Kansas, Lawrence, Kansas 66047, USA
[c]High Throughput Screening Laboratory, University of Kansas, Lawrence, Kansas 66047, USA
[d]Department of Molecular Biology, Medical Biochemistry and Pathology, Laval University Cancer Research Center, Québec City, QC, G1V 0A6, Canada
[e]CHU de Québec Research Center, CHUL Pavilion, Oncology Division, Québec City, QC, G1V 4G2, Canada
[f]Protein Production Group, University of Kansas, Lawrence, Kansas 66047, USA
[g]NYX, New York Structural Biology Center, Upton, NY 11973, USA
[h]Molecular Graphics and Modeling Laboratory and the Computational Chemical Biology Core, University of Kansas, Lawrence, Kansas 66047, USA

[#]Correspondence: arfehr@ku.edu; Tel.: +1- (785) 864-6626 (K.S.)

Running title: SARS-CoV-2 Mac1 removes ADP-ribose from protein

Keywords: Coronavirus, SARS-CoV-2, macrodomain, ADP-ribose, poly-ADP-ribose,

ABSTRACT

Severe acute respiratory syndrome coronavirus 2 (SARS-CoV-2) and other SARS-like-CoVs encode 3 tandem macrodomains within non-structural protein 3 (nsp3). The first macrodomain, Mac1, is conserved throughout CoVs, and binds to and hydrolyzes mono-ADP-ribose (MAR) from target proteins. Mac1 likely counters host-mediated anti-viral ADP-ribosylation, a posttranslational modification that is part of the host response to viral infections. Mac1 is essential for pathogenesis in multiple animal models of CoV infection, implicating it as a virulence factor and potential therapeutic target. Here we report the crystal structure of SARS-CoV-2 Mac1 in complex with ADP-ribose. SARS-CoV-2, SARS-CoV and MERS-CoV Mac1 exhibit similar structural folds and all 3 proteins bound to ADP-ribose with low μM affinities. Importantly, using ADP-ribose detecting binding reagents in both a gel-based assay and novel ELISA assays, we demonstrated de-MARylating activity for all 3 CoV Mac1 proteins, with the SARS-CoV-2 Mac1 protein leading to a more rapid loss of substrate compared to the others. In addition, none of these enzymes could hydrolyze poly-ADP-ribose. We conclude that the SARS-CoV-2 and other CoV Mac1 proteins are MAR-hydrolases with similar functions, indicating that compounds targeting CoV Mac1 proteins may have broad anti-CoV activity.

IMPORTANCE

SARS-CoV-2 has recently emerged into the human population and has led to a worldwide pandemic of COVID-19 that has caused greater than 900 thousand deaths worldwide. With, no currently approved treatments, novel therapeutic strategies are desperately needed. All coronaviruses encode for a highly conserved macrodomain (Mac1) that binds to and removes ADP-ribose adducts from proteins in a dynamic post-translational process increasingly recognized as an important factor that regulates viral infection. The macrodomain is essential for CoV pathogenesis and may be a novel therapeutic target. Thus, understanding its biochemistry and enzyme activity are critical first steps for these efforts. Here we report the crystal structure of SARS-CoV-2 Mac1 in complex with ADP-ribose, and describe its ADP-ribose binding and hydrolysis activities in direct comparison to SARS-CoV and MERS-CoV Mac1 proteins. These results are an important first step for the design and testing of potential therapies targeting this unique protein domain.

INTRODUCTION

The recently emerged pandemic outbreak of COVID-19 is caused by a novel coronavirus named severe acute respiratory syndrome coronavirus 2 (SARS-CoV-2) (1, 2). As of September 16, 2020, this virus has been responsible for ~ 30 million cases of COVID-19 and >900,000 deaths worldwide. SARS-CoV-2 is a member of the lineage B β-CoVs with overall high sequence similarity with other SARS-like CoVs, including SARS-CoV. While most of the genome is >80% similar with SARS-CoV, there are regions where amino acid conservation is significantly lower. As expected, the most divergent proteins in the SARS-CoV-2 genome from SARS-CoV include the Spike glycoprotein and several accessory proteins including 8a (absent), 8b (extended), and 3b (truncated). However, somewhat unexpectedly, several non-structural proteins also show significant divergence from SARS-CoV, including non-structural proteins 3, 4, and 7, which could affect the biology of SARS-CoV-2 (3, 4).

Coronaviruses encode 16 non-structural proteins that are translated from two open reading frames (ORFs), replicase 1a and 1ab (rep1a and rep1ab) (5). The largest non-structural protein is the non-structural protein 3 (nsp3) that encodes for multiple modular protein domains. These domains in SARS-CoV-2 diverge in amino acid sequence from SARS-CoV as much as 30%, and SARS-CoV-2 nsp3 includes a large insertion of 25-41 residues just upstream of the first of three tandem macrodomains (Mac1, Mac2, and Mac3) (Fig. 1A) (3). In addition to this insertion, the individual macrodomains show large amounts of amino acid divergence. Mac1 diverges 28% from SARS-CoV and 59% from MERS-CoV, while Mac2 and Mac3 diverge 24% from SARS-CoV. It is feasible that these significant sequence differences could impact the unique biology of SARS-CoV-2. However, macrodomains have a highly conserved structure, and thus sequence divergence may have little impact on their overall function. Mac1 is present in

all CoVs, unlike Mac2 and Mac3, and early structural and biochemical data demonstrated that it contains a conserved three-layered α/β/α fold and binds to mono-ADP-ribose (MAR) and other related molecules (6-10). This is unlike Mac2 and Mac3, which fail to bind ADP-ribose and instead appear to bind to nucleic acids (11, 12). ADP-ribose is buried in a hydrophobic cleft of Mac1 where the ADP-ribose binds to several highly-conserved residues such as aspartic acid at position 23 (D23) and asparagine at position 41 (N41) of SARS-CoV (Fig. 1B) (6). Mac1 homologs are also found in alphaviruses, Hepatitis E virus, and Rubella virus, and structural analysis of these macrodomains have demonstrated that they are very similar to CoV Mac1 (13, 14). All are members of the larger MacroD-type macrodomain family, which includes human macrodomains Mdo1 and Mdo2 (15).

The CoV Mac1 was originally named ADP-ribose-1”-phosphatase (ADRP) based on data demonstrating that it could remove the phosphate group from ADP-ribose-1”-phosphate (6-8). However, the activity was rather modest, and it was unclear why this would impact a virus infection. More recently it has been demonstrated that CoV Mac1 can hydrolyze the bond between amino acid chains and ADP-ribose molecules (16-18), indicating that it can reverse protein ADP-ribosylation (6, 8). ADP-ribosylation is a post-translational modification catalyzed by ADP-ribosyltransferases (ARTs, also known as PARPs) through transferring an ADP-ribose moiety from NAD^+ onto target proteins (19). The ADP-ribose is transferred as a single unit of MAR, or single units of MAR are transferred consecutively to form a PAR chain. Several Mac1 proteins have been shown to hydrolyze MAR, but have minimal activity towards PAR (16, 17). Several MARylating PARPs are induced by interferon (IFN) and are known to inhibit virus replication, implicating MARylation in the host-response to infection (20).

Several reports have addressed the role of Mac1 on the replication and pathogenesis of CoVs, mostly using the mutation of a highly conserved asparagine to alanine (N41A-SARS-CoV). This mutation abolished the MAR-hydrolase activity of SARS-CoV Mac1 (18). This mutation has minimal effects on CoV replication in transformed cells, but reduces viral load, leads to enhanced IFN production, and strongly attenuates both murine hepatitis virus (MHV) and SARS-CoV in mouse models of infection (7, 18, 21, 22). MHV Mac1 was also required for efficient replication in primary macrophages, which could be partially rescued by the PARP inhibitors XAV-939 and 3-AB or siRNA knockdown of PARP12 or PARP14 (23). These data suggest that Mac1's likely function is to counter PARP-mediated anti-viral ADP-ribosylation (24). Mutations in the alphavirus and HEV macrodomain also have substantial phenotypic effects on virus replication and pathogenesis (16, 25-28). As viral macrodomains are clearly important virulence factors, they are considered to be potential targets for anti-viral therapeutics (24).

Based on the close structural similarities between viral macrodomains, we hypothesized that SARS-CoV-2 Mac1 has similar binding and hydrolysis activity as other CoV Mac1 enzymes. In this study, we determined the crystal structure of the SARS-CoV-2 Mac1 protein bound to ADP-ribose. Binding to and hydrolysis of MAR was tested and directly compared to a human macrodomain (Mdo2) and the SARS-CoV and MERS-CoV Mac1 proteins by several *in vitro* assays. All CoV Mac1 proteins bound to MAR and could remove MAR from a protein substrate. However, the initial rate associated with the loss of substrate was largest for the SARS-CoV-2 Mac1 protein , especially under multi-turnover conditions. In addition, none of these enzymes could remove PAR from a protein substrate. These results indicate that Mac1

121 protein domains likely have similar functions, and will be instrumental in the design and testing

122 of novel therapeutic agents targeting the CoV Mac1 protein domain.

123

RESULTS

Structure of the SARS-CoV-2 Mac1 complexed with ADP-ribose. To create recombinant SARS-CoV-2 Mac1 for structure determination and enzyme assays, nucleotides 3348-3872 of SARS-CoV-2 isolate Wuhan-hu-1 (accession number NC_045512), representing amino acids I1023-K1197 of rep1a, were cloned into a bacterial expression vector containing an N-terminal 6X-His tag and TEV cleavage site. We obtained large amounts (>100 mg) of purified recombinant protein (Fig. S1A). A small amount of this protein was digested by the TEV protease to obtain protein devoid of any extra tags for crystallization and used to obtain crystals from which the structure was determined (Fig. S1B). Our crystallization experiments resulted in the same crystal form (needle clusters) from several conditions, but only when ADP-ribose was added to the protein. This represents an additional crystal form ($P2_1$) amongst the recently determined SARS-CoV-2 macrodomain structures (29-31).

The structure of SARS-CoV-2 Mac1 complexed with ADP-ribose was obtained using X-ray diffraction data to 2.2 Å resolution and contained four molecules in the asymmetric unit that were nearly identical. The polypeptide chains could be traced from V3-M171 for subunits A/C and V3-K172 for subunits B/D. Superposition of subunits B-D onto subunit A (169 residues aligned) yielded RMSD deviations of 0.17 Å, 0.17 Å and 0.18 Å respectively between Cα atoms. As such, subunit A was used for the majority of the structure analysis described herein. The SARS-CoV-2 Mac1 protein adopted a fold consistent with the MacroD sub-family of macrodomains that contains a core composed of a mixed arrangement of 7 β-sheets (parallel and antiparallel) that are flanked by 6 α-helices (Fig. 2A-B).

As mentioned above, apo crystals were never observed for our construct, though the apo structure has been solved by researchers at The Center for Structural Genomics of Infectious

Diseases (PDB 6WEN) (30) and the University of Wisconsin-Milwaukee (PDB 6WEY) (32). Further analysis of the amino acid sequences used for expression and purification revealed that our construct had 5 additional residues at the C-terminus (MKSEK) and differs slightly at the N-terminus as well (GIE vs GE) relative to 6WEN. In addition, the sequence used to obtain the structure of 6WEY is slightly shorter than SARS-CoV-2 Mac1 at both the N and C-terminal regions (Fig. S2A). To assess the effect of these additional residues on crystallization, chain B of the SARS-CoV-2 Mac1, which was traced to residue K172, was superimposed onto subunit A of PDB 6W02 (31), a previously determined structure of ADP-ribose bound SARS-CoV-2 Mac1. Analysis of the crystal packing of 6W02 indicates that the additional residues at the C-terminus would clash with symmetry related molecules (Fig. S2B). This suggests that the presence of these extra residues at the C-terminus likely prevented the generation of the more tightly packed crystal forms obtained for 6W02 and 6WEY, which diffracted to high resolution.

The ADP-ribose binding pocket contained large regions of positive electron density consistent with the docking of ADP-ribose (Fig. 3A). The adenine forms two hydrogen bonds with D22-I23, which makes up a small loop between β2 and the N-terminal half of α1. The side chain of D22 interacts with N6, while the backbone nitrogen atom of I23 interacts with N1, in a very similar fashion to the SARS-CoV macrodomain (6). This aspartic acid is known to be critical for ADP-ribose binding for alphavirus macrodomains (26, 27). A large number of contacts are made in the highly conserved loop between β3 and α2 which includes many highly-conserved residues, including a GGG (motif) and N40, which is completely conserved in all enzymatically active macrodomains (33). N40 is positioned to make hydrogen bonds with the 3' OH groups of the distal ribose, as well as a conserved water molecule (Fig. 3B-C). K44 and G46 also make hydrogen bonds with the 2' OH of the distal ribose, G48 makes contact with the 1'

OH and a water that resides near the catalytic site, while the backbone nitrogen atom of V49 hydrogen bonds with the α-phosphate. The other major interactions with ADP-ribose occur in another highly conserved region consisting of residues G130, I131, and F132 that are in the loop between β6 and α5 (Fig. 3B). The α-phosphate accepts a hydrogen bond from the nitrogen atom of I131, while the β-phosphate accepts hydrogen bonds from the backbone nitrogen atom of G130 and F132. The phenyl ring of F132 may make van der Waals interactions with the distal ribose to stabilize it, which may contribute to binding and hydrolysis (34). Loops β3-α2 and β6-α5 are connected by an isoleucine bridge that forms a narrow channel around the diphosphate which helps position the terminal ribose for water-mediated catalysis (6). Of all these residues, is not exactly clear which ones are important for ADP-ribose binding, hydrolysis, or both. Additionally, a network of direct contacts of ADP-ribose to solvent along with water mediated contacts to the protein are shown (Fig. 3C).

Comparison of SARS-CoV-2 Mac1 with other CoV macrodomain structures. We next sought to compare the SARS-CoV-2 Mac1 to other deposited structures of this protein. Superposition with Apo (6WEN) and ADP-ribose complexed protein (6W02) yielded RMSD of 0.48 Å (168 residues) and 0.37 Å (165 residues), respectively, indicating a high degree of similarity (Fig. S3A-B). Comparison of the ADP-ribose binding site of SARS-CoV-2 Mac1 with that of the apo structure (6WEN) revealed minor conformational differences in order to accommodate ADP-ribose binding. The loop between β3 and α2 (H45-V49) undergoes a change in conformation and the sidechain of F132 is moved out of the ADP-ribose binding site (Fig. S3C). Our ADP-ribose bound structure is nearly identical to 6W02, except for slight deviations in the β3-α2 loop and an altered conformation of F156, where the aryl ring of F156 is moved closer to the adenine ring (Fig. S3 C-D). However, this is likely a result of crystal packing as

193 F156 adopts this conformation in each subunit and would likely clash with subunit residues
194 related by either crystallographic or non-crystallographic symmetry.

195 We next compared the ADP-ribose bound SARS-CoV-2 Mac1 structure with that of
196 SARS-CoV (PDB 2FAV) (6) and MERS-CoV (PDB 5HOL) (35) Mac1 proteins. Superposition
197 yielded RMSD deviations of 0.71 Å (166 residues) and 1.06 Å (161 residues) for 2FAV and
198 5HOL, respectively. Additionally, the ADP-ribose binding mode in the SARS-CoV and SARS-
199 CoV-2 structures almost perfectly superimposed (Fig. 4A-D). The conserved aspartic acid
200 residue (D22, SARS-CoV-2) that binds to adenine, is localized in a similar region in all 3
201 proteins although there are slight differences in the rotamers about the Cβ-Cγ bond. The angles
202 between the mean planes defined by the OD1, CG and OD2 atoms relative to SARS-CoV-2
203 Mac1 is 23.1° and 46.5° for the SARS-CoV and MERS-CoV Mac1 structures, respectively.
204 Another notable difference is that SARS-CoV and SARS-CoV-2 macrodomains have an
205 isoleucine (I23) following this aspartic acid while MERS-CoV has an alanine (A22). Conversely,
206 SARS-CoV-2 and SARS-CoV Mac1 have a valine instead of an isoleucine immediately
207 following the GGG motif (V49/I48). From these structures it appears that having two isoleucines
208 in this location would clash, and that lineage B and lineage C β-CoVs has evolved in unique
209 ways to create space in this pocket (Fig. 4D and data not shown). Despite these small differences
210 in local structure, the overall structure of CoV Mac1 domains remain remarkably conserved, and
211 indicates they likely have similar biochemical activities and biological functions.

212 **SARS-CoV, SARS-CoV-2, and MERS-CoV bind to ADP-ribose with similar**
213 **affinities.** To determine if the CoV macrodomains had any noticeable differences in their ability
214 to bind ADP-ribose, we performed isothermal titration calorimetry (ITC), which measures the
215 energy released or absorbed during a binding reaction. Macrodomain proteins from human

(Mdo2), SARS-CoV, MERS-CoV, and SARS-CoV-2 were purified (Fig. S1A) and tested for their affinity to ADP-ribose. All CoV Mac1 proteins bound to ADP-ribose with low micromolar affinity (7-16 μM), while human Mdo2 bound with an affinity about 10-times stronger (~220 nM) (Fig. 5A-B). As a control we tested the ability of the MERS-CoV macrodomain to bind to ATP, and only observed minimal binding with mM affinity (data not shown). At higher concentrations, the SARS-CoV-2 macrodomain caused a slightly endothermic reaction, potentially the result of protein aggregation or a change in conformation (Fig. 5A). The MERS-CoV Mac1 had a greater affinity for ADP-ribose than SARS-CoV or SARS-CoV-2 Mac1 in the ITC assay (Fig. 5A-B), however, our results found the differences between these macrodomain proteins to be much closer than previously reported (9). As an alternate method to confirm ADP-ribose binding, we conducted a thermal shift assay. All 4 macrodomains tested denatured at higher temperatures with the addition of ADP-ribose (Fig. S4). We conclude that lineage B and lineage C β-CoV Mac1 proteins bind to ADP-ribose with similar affinities.

CoV macrodomains are MAR-hydrolases. To examine the MAR-hydrolase activity of CoV Mac1, we first tested the viability of using ADP-ribose binding reagents to detect MARylated protein. Previously, radiolabeled NAD^+ has been the primary method used to label MARylated protein (16, 17). To create a MARylated substrate, the catalytic domain of the PARP10 (GST-PARP10 CD) protein was incubated with NAD^+, leading to its automodification. PARP10 CD is a standard substrate that has been used extensively in the field to analyze the activity of macrodomains (16, 18, 26, 27). PARP10 is highly upregulated upon CoV infection (23, 36) and is known to primarily auto-MARylate itself on acidic residues, which are the targets of the MacroD2 class of macrodomains (27). We then tested a panel of anti-MAR, anti-PAR, or both anti-MAR and anti-PAR binding reagents/antibodies for the ability to detect MARylated

239 PARP10 by immunoblot. The anti-MAR and anti-MAR/PAR binding reagents, but not anti-PAR
240 antibody, bound to MARylated PARP10 (Fig. S5). Therefore, in this work we utilized the anti-
241 MAR binding reagent to detect MARylated PARP10.
242 We next tested the ability of SARS-CoV-2 Mac1 to remove ADP-ribose from
243 MARylated PARP10. SARS-CoV-2 Mac1 and MARylated PARP10 were incubated at
244 equimolar amounts of protein at 37°C and the reaction was stopped at 5, 10, 20, 30, 45 or 60
245 minutes (Fig. 6A). As a control, MARylated PARP10 was incubated alone at 37°C and collected
246 at similar time points (Fig. 6A and Fig. S6). Each reaction had equivalent amounts of
247 MARylated PARP10 and Mac1 which was confirmed by Coomassie Blue staining (Fig. 6A). An
248 immediate reduction of more than 50% band intensity was observed within five minutes, and the
249 ADP-ribose modification was nearly completely removed by SARS-CoV-2 Mac1 within 30
250 minutes (Fig. 6A). The MARylated PAPR10 bands intensities were calculated, plotted, and were
251 fit using non-linear regression (Fig. 6B). This result indicates that the SARS-CoV-2 Mac1
252 protein is a mono-ADP-ribosylhydrolase enzyme.
253 Next, we compared the MAR-hydrolase activity of Mac1 proteins from SARS-CoV-2,
254 SARS-CoV, and MERS-CoV and human (i.e., Mdo2). Specifically, we monitored the time-
255 dependent loss of substrate using immunoblotting (Fig. 6C) under equimolar (i.e., 1 μM
256 [Mac1]:1 μM [substrate]) and multiple-turnover conditions (i.e., 0.5 μM [substrate]:0.1 μM
257 [Mac1] and 1.0 μM [substrate]:0.1 μM [Mac1]), with total protein amounts confirmed by
258 Coomassie blue staining (Fig. S7). The resulting substrate decay plots (Fig. 6D) were fit using
259 non-linear regression to determine the initial rate (k) of substrate decay. Our results indicate that
260 the three CoV Mac1 proteins give rise to similar, but not identical, values of k (Fig. 6D). The
261 SARS-CoV-2 Mac1 protein has a greater k than the SARS-CoV or MERS-CoV Mac1 proteins,

262 especially under multiple-turnover conditions, and all 3 viral macrodomains gave rise to a more
263 rapid loss of substrate than the human Mdo2 enzyme (Fig. 6F). However, further enzymatic
264 analyses of these proteins are warranted to more thoroughly understand their kinetics and
265 binding affinities associated with various MARylated substrates.

266 **CoV Mac1 proteins do not hydrolyze PAR.** To determine if the CoV Mac1 proteins
267 could remove PAR from proteins, we incubated these proteins with an auto-PARylated PARP1
268 protein. PARP1 was incubated with increasing concentrations of NAD^+ to create a range of
269 modification levels (Fig. S8). We incubated both partially and heavily modified PARP1 with all
270 four macrodomains and PARG as a positive control for 1 hour. While PARG completely
271 removed PAR, none of the macrodomain proteins removed PAR chains from PARP1 (Fig. 7).
272 We conclude that macrodomain proteins are unable to remove PAR from an automodified
273 PARP1 protein under these conditions.

274 **ELISA assays can be used to measure ADP-ribosylhydrolase activity of**
275 **macrodomains.** Gel based assays as described above suffer from significant limitations in the
276 number of samples that can be done at once. A higher throughput assay will be needed to more
277 thoroughly investigate the activity of these enzymes and to screen for inhibitor compounds.
278 Based on the success of our antibody-based detection of MAR, we developed an ELISA assay
279 that has a similar ability to detect de-MARylation as our gel-based assay, but with the ability to
280 do so in a higher throughput manner (Fig. 8A). First, MARylated PARP10 was added to ELISA
281 plates. Next, the wells were washed and then incubated with different concentrations of the
282 SARS-CoV-2 Mac1 protein for 60 min. After incubation, the wells were washed and treated with
283 anti-MAR binding reagent, followed by HRP-conjugated secondary antibody and the detection
284 reagent. As controls, we detected MARylated and non-MARylated PARP10 proteins bound to

285 glutathione plates with anti-GST antibody and anti-MAR binding reagents and their
286 corresponding secondary antibodies (Fig. 8B). SARS-CoV-2 Mac1 was able to remove MAR
287 signal in a dose-dependent manner and plotted to a linear non-regression fitted line (Fig. 8C).
288 Based on these results, we believe that this ELISA assay will be a useful tool for screening
289 potential inhibitors of macrodomain proteins.

DISCUSSION

Here we report the crystal structure of SARS-CoV-2 Mac1 and its enzyme activity *in vitro*. Structurally, it has a conserved three-layered α/β/α fold typical of the MacroD family of macrodomains, and is extremely similar to other CoV Mac1 proteins (Fig. 2-4). The conserved CoV macrodomain (Mac1) was initially described as an ADP-ribose-1”-phosphatase (ADRP), as it was shown to be structurally similar to yeast enzymes that have this enzymatic activity (37). Early biochemical studies confirmed this activity for CoV Mac1, though its phosphatase activity for ADP-ribose-1”-phosphate was rather modest (6-8). Later, it was shown that mammalian macrodomain proteins could remove ADP-ribose from protein substrates, indicating protein de-ADP-ribosylation as a more likely function for the viral macrodomains (33, 38, 39). Shortly thereafter, the SARS-CoV, hCoV-229E, FIPV, several alphavirus, and the hepatitis E virus macrodomains were demonstrated to have de-ADP-ribosylating activity (16-18). However, this activity has not yet been reported for the MERS-CoV or SARS-CoV-2 Mac1 protein.

In this study, we show that the Mac1 proteins from SARS-CoV, MERS-CoV and SARS-CoV-2 hydrolyze MAR from a protein substrate (Fig. 6). Their enzymatic activities were similar despite sequence divergence of almost 60% between SARS-CoV-2 and MERS-CoV. However, the initial rate associated with the loss of substrate was largest for the SARS-CoV-2 Mac1 protein, particularly under multiple-turnover conditions. It is unclear what structural or sequence differences may account for the increased activity of the SARS-CoV-2 Mac1 protein under these conditions, especially considering the pronounced structurally similarities between these proteins, specifically the SARS-CoV Mac1 (0.71 Å RMSD). It is also unclear if these differences would matter in the context of the virus infection, as the relative concentrations of Mac1 and its substrate during infection is not known. We also compared these activities to the human Mdo2

313 macrodomain. Mdo2 had a greater affinity for ADP-ribose than the viral enzymes, but had
314 significantly reduced enzyme activity in our experiments. Due to its high affinity for ADP-
315 ribose, it is possible that the Mdo2 protein was partially inhibited by rebinding to the MAR
316 product in these assays. Regardless, these results suggest that the human and viral proteins likely
317 have structural differences that alter their biochemical activities *in vitro*, indicating that it may be
318 possible to create viral macrodomain inhibitors that don't impact the human macrodomains. We
319 also compared the ability of these macrodomain proteins to hydrolyze PAR. None of the
320 macrodomains were able to hydrolyze either partially or heavily modified PARP1, further
321 demonstrating that the primary enzymatic activity of these proteins is to hydrolyze MAR (Fig.
322 7).

323 When analyzing viral macrodomain sequences, it is clear that they have at least 3 highly
324 conserved regions (Fig. 1B)(24). The first region includes the NAAN (37-40) and GGG (residues
325 46-48) motifs in the loop between β3 and α2. The second domain includes a GIF (residues 130-
326 132) motif in the loop between β6 and α5. The final conserved region is a VGP (residues 96-98)
327 motif at the end of β5 and extends into the loop between β5 and α4. Both of the first two
328 domains have well defined interactions with ADP-ribose (Fig. 3). However, no one has
329 addressed the role of the VGP residues, though our structure indicates that the glycine may
330 interact with a water molecule that makes contact with the β-phosphate. Identifying residues that
331 directly contribute to ADP-ribose binding, hydrolysis, or both by CoV Mac1 proteins will be
332 critical to determining the specific roles of ADP-ribose binding and hydrolysis in CoV
333 replication and pathogenesis.

334 While all previous studies of macrodomain de-ADP-ribosylation have primarily used
335 radiolabeled substrate, we obtained highly repeatable and robust data utilizing ADP-ribose

binding reagents designed to specifically recognize MAR (40, 41). The use of these binding reagents should enhance the feasibility of this assay for many labs that are not equipped for radioactive work. Utilizing these binding reagents, we further developed an ELISA assay for de-MARylation that has the ability to dramatically increase the number of samples that can be analyzed compared to the gel-based assay. To our knowledge, previously developed ELISA assays were used to measure ADP-ribosyltransferase activities (42) but no ELISA has been established to test the ADP-ribosylhydrolase activity of macrodomain proteins. This ELISA assay should be useful to those in the field to screen compounds for macrodomain inhibitors that could be either valuable research tools or potential therapeutics.

The functional importance of the CoV Mac1 domain has been demonstrated in several reports, mostly utilizing the mutation of a highly conserved asparagine that mediates contact with the distal ribose (Fig. 3B) (18, 21, 22). However, the physiological relevance of Mac1 during SARS-CoV-2 infection has yet to be determined. In addition, the proteins that are targeted by the CoV Mac1 for de-ADP-ribosylation remains unknown. Unfortunately, there are no known compounds that inhibit this domain that could help identify the functions of this protein during infection. The outbreak of COVID-19 has illustrated an urgent need for developing multiple therapeutic drugs targeting conserved coronavirus proteins. Mac1 appears to be an ideal candidate for further drug development based on: *i)* its highly conserved structure and biochemical activities within CoVs; and *ii)* its importance for multiple CoVs to cause disease. Targeting Mac1 may also have the benefit of enhancing the innate immune response, as we have shown that Mac1 is required for some CoVs to block IFN production (18, 23). Considering that Mac1 proteins from divergent αCoVs such as 229E and FIPV also have de-ADP-ribosylating activity (16, 17), it is possible that compounds targeting Mac1 could prevent disease caused by

359 of wide variety of CoV, including those of veterinary importance like porcine epidemic diarrhea
360 virus (PEDV). Additionally, compounds that inhibit Mac1 in combination with the structure
361 could help identify the mechanisms it uses to bind to its biologically relevant protein substrates,
362 remove ADP-ribose from these proteins, and potentially define the precise function for Mac1 in
363 SARS-CoV-2 replication and pathogenesis. In conclusion, the results described here will be
364 critical for the design and development of highly-specific Mac1 inhibitors that could be used
365 therapeutically to mitigate COVID-19 or future CoV outbreaks.
366

METHODS

Plasmids

The SARS-CoV macrodomain (Mac1) (residues 1000-1172 of pp1a) was cloned into the pET21a+ expression vector with an N-terminal His tag. The MERS-CoV Mac1 (residues 1110-1273 of pp1a) was also cloned into pET21a+ with a C-terminal His tag. SARS-CoV-2 Mac1 (residues 1023-1197 of pp1a) was cloned into the pET30a+ expression vector with an N-terminal His tag and a TEV cleavage site (Synbio). The pETM-CN Mdo2 Mac1 (residues 7-243) expression vector with an N-terminal His-TEV-V5 tag and the pGEX4T-PARP10-CD (residues 818-1025) expression vector with an N-terminal GST tag were previously described (33). All plasmids were confirmed by restriction digest, PCR, and direct sequencing.

Protein Expression and Purification

A single colony of *E. coli* cells (C41(DE3)) containing plasmids harboring the constructs of the macrodomain proteins was inoculated into 10 mL LB media and grown overnight at 37°C with shaking at 250 rpm. The overnight culture was transferred to a shaker flask containing 2X 1L TB media at 37°C until the OD600 reached 0.7. The proteins were either induced with 0.4 mM IPTG at 37°C for 3 hours, or 17°C for 20 hours. Cells were pelleted at 3500 × g for 10 min and frozen at -80°C. Frozen cells were thawed at room temperature, resuspended in 50 mM Tris (pH 7.6), 150 mM NaCl, and sonicated using the following cycle parameters: Amplitude: 50%, Pulse length: 30 seconds, Number of pulses: 12, while incubating on ice for >1min between pulses. The soluble fraction was obtained by centrifuging the cell lysate at 45,450 × g for 30 minutes at 4°C. The expressed soluble proteins were purified by affinity chromatography using a 5 ml prepacked HisTrap HP column on an AKTA Pure protein purification system (GE Healthcare). The fractions were further purified by size-exclusion chromatography (SEC) with a

Superdex 75 10/300 GL column equilibrated with 20mM Tris (pH 8.0), 150 mM NaCl and the protein sized as a monomer relative to the column calibration standards. To cleave off the His tag from the SARS-CoV-2 Mac1, purified TEV protease was added to purified SARS-CoV-2 Mac1 protein at a ratio of 1:10 (w/w), and then passed back through the Ni-NTA HP column. Protein was collected in the flow through and equilibrated with 20 mM Tris (pH 8.0), 150 mM NaCl. The SARS-CoV-2 Mac1, free from the N-terminal 6X-His tag, was used for subsequent crystallization experiments.

For the PARP10-CD protein, the cell pellet was resuspended in 50 mM Tris-HCl (pH 8.0), 500 mM NaCl, 0.1mM EDTA, 25% glycerol, 1 mM DTT and sonicated as described above. The cell lysate was incubated with 10 ml of Glutathione Sepharose 4B resin from GE Healthcare, equilibrated with the same buffer for 2 hours, then applied to a gravity flow column to allow unbound proteins to flow through. The column was washed with the resuspension buffer till the absorbance at 280 nm reached baseline. The bound protein was eluted out of the column with resuspension buffer containing 20 mM reduced glutathione and then dialyzed back into the resuspension buffer overnight at 4°C.

Isothermal Titration Calorimetry

All ITC titrations were performed on a MicroCal PEAQ-ITC instrument (Malvern Pananalytical Inc., MA). All reactions were performed in 20 mM Tris pH 7.5, 150 mM NaCl using 100 μM of all macrodomain proteins at 25°C. Titration of 2 mM ADP-ribose or ATP (MilliporeSigma) contained in the stirring syringe included a single 0.4 μL injection, followed by 18 consecutive injections of 2 μL. Data analysis of thermograms was analyzed using one set of binding sites model of the MicroCal ITC software to obtain all fitting model parameters for the experiments.

Differential Scanning Fluorimetry (DSF)

Thermal shift assay with DSF involved use of LightCycler® 480 Instrument (Roche Diagnostics). In total, a 15 µL mixture containing 8X SYPRO Orange (Invitrogen), and 10 µM macrodomain protein in buffer containing 20 mM Hepes, NaOH, pH 7.5 and various concentrations of ADP-ribose were mixed on ice in 384-well PCR plate (Roche). Fluorescent signals were measured from 25 to 95 °C in 0.2 °C/30-s steps (excitation, 470-505 nm; detection, 540-700 nm). The main measurements were carried out in triplicate. Data evaluation and Tm determination involved use of the Roche LightCycler® 480 Protein Melting Analysis software, and data fitting calculations involved the use of single site binding curve analysis on Graphpad Prism.

MAR Hydrolase Assays

Automodification of PARP10-CD protein: A 10 µM solution of purified PAPR10-CD protein was incubated for 20 minutes at 37ºC with 1 mM final concentration of β-Nicotinamide Adenine Dinucleotide (β NAD^+) (Millipore-Sigma) in a reaction buffer (50 mM HEPES, 150 mM NaCl, 0.2 mM DTT, and 0.02% NP-40). MARylated PARP10 was aliquoted and stored at -80ºC.

PAPR10-CD ADP-ribose hydrolysis: All reactions were performed at 37ºC for the designated time. A 1 µM solution of MARylated PARP10-CD and purified Mac1 protein was added in the reaction buffer (50 mM HEPES, 150 mM NaCl, 0.2 mM DTT, and 0.02% NP-40). The reaction was stopped with addition of 2X Laemmli sample buffer containing 10% β-mercaptoethanol.

Protein samples were heated at 95ºC for 5 minutes before loading and separated onto SDS-PAGE cassette (Thermo Fisher Scientific Bolt™ 4-12% Bis-Tris Plus Gels) in MES

running buffer. For direct protein detection, the SDS-PAGE gel was stained using InstantBlue® Protein Stain (Expedeon). For immunoblotting, the separated proteins were transferred onto polyvinylidene difluoride (PVDF) membrane using iBlot™ 2 Dry Blotting System (ThermoFisher Scientific). The blot was blocked with 5% skim milk in PBS containing 0.05% Tween-20 and probed with anti-mono or poly ADP-ribose binding reagents/antibodies MABE1076 (α-MAR), MABC547 (α-PAR), MABE1075 (α-MAR/PAR) (Millipore-Sigma) and anti-GST tag monoclonal antibody MA4-004 (ThermoFisher Scientific). The primary antibodies were detected with secondary infrared anti-rabbit and anti-mouse antibodies (LI-COR Biosciences). All immunoblots were visualized using Odyssey® CLx Imaging System (LI-COR Biosciences). The images were quantitated using Image J (National Institutes for Health (NIH)) or Image Studio software.

Kinetic analysis of ADP-ribose hydrolysis: To quantify the initial rate (k) of substrate decay associated with the four macrodomains, each data set represented in the substrate decay immunoblots in Fig. 6C, were fitted to a decaying exponential with the following functional form: $([S]_{initial}\text{-}[S]_{final})e^{(-[k/[S]_{initial})t]}+[S]_{final}$ (Mathematica 12, Wolfram Alpha). The decay plots and resulting values for the fitted parameter k along with statistic uncertainty (SD) are shown in Fig. 6D.

ELISA-based MAR hydrolysis: ELISA Well-Coated™ Glutathione plates (G-Biosciences, USA) were washed with phosphate-buffered saline (PBS) containing 0.05% Tween-20 (PBS-T) and incubated with 50 µL of 100 nM automodified MARylated PARP10-CD in PBS for one hour under room temperature. Following four washes with PBS-T, variable concentrations of SARS-CoV-2 Mac1 were incubated with MARylated PARP10-CD for 60 minutes at 37ºC. Purified macrodomains were 2-fold serially diluted starting at 100 nM in reaction buffer prior to

addition to MARylated PARP10-CD. Subsequently, ELISA wells were washed four times with PBS-T and incubated with 50 µL/well of anti-GST (Invitrogen MA4-004) or anti-MAR (Millipore-Sigma MAB1076) diluted 1:5,000 in 5 mg/ml BSA in PBS-T (BSA5-PBS-T) for 1 hour at room temperature. After four additional washes with PBS-T, each well was incubated with 50 µL diluted 1:5,000 in BSA5-PBS-T of anti-rabbit-HRP (SouthernBiotech, USA) or anti-mouse-HRP (Rockland Immunochemicals, USA) conjugate for 1 hour at room temperature. The plate was washed four times with PBS-T and 100 µL of TMB peroxidase substrate solution (SouthernBiotech, USA) was added to each well and incubated for 10 minutes. The peroxidase reaction was stopped with 50 µL per well of 1 M HCl before proceeding to reading. Absorbance was measured at 450 nm and subtracted from 620 nm using Biotek Powerwave XS plate reader (BioTek). As controls, MARylated PARP10-CD and non-MARylated PARP10 were detected with both anti-MAR and anti-GST antibodies. The absorbance of non-MARylated PARP10-CD detected with anti-MAR antibody was used to establish the background signal. The % signal remaining was calculated by dividing the experimental signal (+ enzyme) minus background by the control (no enzyme) minus the background.

PAR Hydrolase Assay

Automodification of PARP1 protein: PARP1 was incubated with increasing concentrations of NAD^+ to generate a range of PARP1 automodification levels. Highly purified human 6X-His-PARP1 (43) (5 µg) was incubated for 30 min at 30°C in a reaction buffer containing 100 mM Tris-HCl pH 8.0, 10 mM $MgCl_2$, 10% (v/v) glycerol, 10 mM DTT, 0 to 500 µM NAD+, 10% (v/v) ethanol and 25 µg/mL calf thymus activated DNA (Sigma-Aldrich).

PARP1 ADP-ribose hydrolysis: To evaluate the PAR hydrolase activity of CoV macrodomains, 200 ng of slightly automodified PARP1 with 5 µM NAD^+ or highly

automodified with 500 μM NAD^+ were used as substrates for the de-PARylation assays. Recombinant macrodomain protein (1 μg) was supplemented to the reaction buffer (100 mM Tris-HCl pH 8.0, 10% (v/v) glycerol and 10 mM DTT) containing automodified PARP1 and incubated for 1 hour at 37°C. Recombinant PARG (1 μg) was used as a positive control for PAR erasing (44). Reaction mixtures were resolved on 4–12% Criterion™ XT Bis-Tris protein gels, transferred onto nitrocellulose membrane and probed with the anti-PAR polyclonal antibody 96-10.

Structure Determination

Crystallization and Data Collection: Purified SARS-CoV-2 Mac1 in 150 mM NaCl, 20 mM Tris pH 8.0 was concentrated to 13.8 mg/mL for crystallization screening. All crystallization experiments were setup using an NT8 drop-setting robot (Formulatrix Inc.) and UVXPO MRC (Molecular Dimensions) sitting drop vapor diffusion plates at 18°C. 100 nL of protein and 100 nL crystallization solution were dispensed and equilibrated against 50 μL of the latter. The SARS-CoV-2 Mac1 complex with ADP-ribose was prepared by adding the ligand, from a 100 mM stock in water, to the protein at a final concentration of 2 mM. Crystals that were obtained in 1-2 days from the Salt Rx HT screen (Hampton Research) condition E10 (1.8 M NaH_2PO_4/K_2HPO_4, pH 8.2). Refinement screening was conducted using the additive screen HT (Hampton Research) by supplementing 10% of each additive to the Salt Rx HT E10 condition in a new 96-well UVXPO crystallization plate. The crystals used for data collection were obtained from Salt Rx HT E10 supplemented with 0.1 M NDSB-256 from the additive screen (Fig. S1). Samples were transferred to a fresh drop composed of 80% crystallization solution and 20% (v/v) PEG 200 and stored in liquid nitrogen. X-ray diffraction data were collected at the

Advanced Photon Source, IMCA-CAT beamline 17-ID using a Dectris Eiger 2X 9M pixel array detector.

Structure Solution and Refinement: Intensities were integrated using XDS (45, 46) via Autoproc (47) and the Laue class analysis and data scaling were performed with Aimless (48). Notably, a pseudo-translational symmetry peak was observed at (0, 0.31 0.5) that was 44.6% of the origin. Structure solution was conducted by molecular replacement with Phaser (49) using a previously determined structure of ADP-ribose bound SARS-CoV-2 Mac1 (PDB 6W02) as the search model. The top solution was obtained in the space group $P2_1$ with four molecules in the asymmetric unit. Structure refinement and manual model building were conducted with Phenix (50) and Coot (51) respectively. Disordered side chains were truncated to the point for which electron density could be observed. Structure validation was conducted with Molprobity (52) and figures were prepared using the CCP4MG package (53). Superposition of the macrodomain structures was conducted with GESAMT (54).

Statistical Analysis

All statistical analyses were done using an unpaired two-tailed student's t-test to assess differences in mean values between groups, and graphs are expressed as mean ±SD. Significant p values are denoted with *$p \leq 0.05$.

ACCESSION CODES

The coordinates and structure factors for SARS-CoV-2 Mac1 were deposited to the Worldwide Protein Databank (wwPDB) with the accession code 6WOJ.

ACKNOWLEDGEMENTS

We'd like to thank Ivan Ahel and Gytis Jankevicius (Oxford University) for providing protein expression plasmids; John Pascal (University of Montreal) and Marie-France Langelier

527 (Universite de Montreal) for providing PARP1; and Wenqing Xu (University of Washington) for
528 providing PARG. This research was funded by the National Institutes of Health (NIH) grant
529 numbers P20 GM113117, P30GM110761, and AI134993-01, and University of Kansas start-up
530 funds to A.R.F, and the Canadian Institutes of Health Research grant number MOP-418863 to
531 G.G.P. Use of the IMCA-CAT beamline 17-ID at the Advanced Photon Source was supported by
532 the companies of the Industrial Macromolecular Crystallography Association through a contract
533 with Hauptman-Woodward Medical Research Institute. Use of the Advanced Photon Source was
534 supported by the U.S. Department of Energy, Office of Science, Office of Basic Energy
535 Sciences, under Contract No. DE-AC02-06CH11357.
536

AUTHOR CONTRIBUTIONS

Conceptualization: ARF, YMOA, GGP

Data curation: YMOA, SL, JPG, ARF, EDH

Formal analysis: YMOA, DKJ, AR, SL, ARF, EDH

Funding acquisition: GGP, SL, ARF

Investigation: YMOA, MMK, AR, JPG, LN, PM, KPB

Methodology: YMOA, GGP, AR, JPG, EDH, SL, ARF

Project administration: GGP, SL, ARF

Resources: AR, SL, PG, ARF

Supervision: AR, GGP, SL ARF

Validation: YMOA, SL, AR, JPG, GGP, ARF

Visualization: YMOA, ARF, AR, SL, JPG

Writing – original draft: YMOA, SL, ARF

Writing – review & editing: all authors

552 **REFERENCES**
553
554 1. Zhou P, Yang XL, Wang XG, Hu B, Zhang L, Zhang W, Si HR, Zhu Y, Li B, Huang CL,
555 Chen HD, Chen J, Luo Y, Guo H, Jiang RD, Liu MQ, Chen Y, Shen XR, Wang X, Zheng
556 XS, Zhao K, Chen QJ, Deng F, Liu LL, Yan B, Zhan FX, Wang YY, Xiao GF, Shi ZL.
557 2020. A pneumonia outbreak associated with a new coronavirus of probable bat origin.
558 Nature 579:270-273.
559 2. Coronaviridae Study Group of the International Committee on Taxonomy of V. 2020.
560 The species Severe acute respiratory syndrome-related coronavirus: classifying 2019-
561 nCoV and naming it SARS-CoV-2. Nat Microbiol 5:536-544.
562 3. Srinivasan S, Cui H, Gao Z, Liu M, Lu S, Mkandawire W, Narykov O, Sun M, Korkin D.
563 2020. Structural Genomics of SARS-CoV-2 Indicates Evolutionary Conserved
564 Functional Regions of Viral Proteins. Viruses 12:360.
565 4. Wu C, Liu Y, Yang Y, Zhang P, Zhong W, Wang Y, Wang Q, Xu Y, Li M, Li X, Zheng
566 M, Chen L, Li H. 2020. Analysis of therapeutic targets for SARS-CoV-2 and discovery
567 of potential drugs by computational methods. Acta Pharm Sin B
568 doi:10.1016/j.apsb.2020.02.008.
569 5. Fehr AR, Perlman S. 2015. Coronaviruses: An Overview of Their Replication and
570 Pathogenesis, p 1-23. *In* Maier HJ, Bickerton E, Britton P (ed), Coronaviruses, vol 1282.
571 Springer New York.
572 6. Egloff MP, Malet H, Putics A, Heinonen M, Dutartre H, Frangeul A, Gruez A,
573 Campanacci V, Cambillau C, Ziebuhr J, Ahola T, Canard B. 2006. Structural and
574 functional basis for ADP-ribose and poly(ADP-ribose) binding by viral macro domains. J
575 Virol 80:8493-502.
576 7. Putics A, Filipowicz W, Hall J, Gorbalenya AE, Ziebuhr J. 2005. ADP-ribose-1"-
577 monophosphatase: a conserved coronavirus enzyme that is dispensable for viral
578 replication in tissue culture. J Virol 79:12721-31.
579 8. Saikatendu KS, Joseph JS, Subramanian V, Clayton T, Griffith M, Moy K, Velasquez J,
580 Neuman BW, Buchmeier MJ, Stevens RC, Kuhn P. 2005. Structural basis of severe acute
581 respiratory syndrome coronavirus ADP-ribose-1"-phosphate dephosphorylation by a
582 conserved domain of nsP3. Structure 13:1665-75.
583 9. Cho CC, Lin MH, Chuang CY, Hsu CH. 2016. Macro Domain from Middle East
584 Respiratory Syndrome Coronavirus (MERS-CoV) Is an Efficient ADP-ribose Binding
585 Module: CRYSTAL STRUCTURE AND BIOCHEMICAL STUDIES. J Biol Chem
586 291:4894-902.
587 10. Xu Y, Cong L, Chen C, Wei L, Zhao Q, Xu X, Ma Y, Bartlam M, Rao Z. 2009. Crystal
588 structures of two coronavirus ADP-ribose-1"-monophosphatases and their complexes
589 with ADP-Ribose: a systematic structural analysis of the viral ADRP domain. J Virol
590 83:1083-92.
591 11. Tan J, Vonrhein C, Smart OS, Bricogne G, Bollati M, Kusov Y, Hansen G, Mesters JR,
592 Schmidt CL, Hilgenfeld R. 2009. The SARS-unique domain (SUD) of SARS coronavirus
593 contains two macrodomains that bind G-quadruplexes. PLoS Pathog 5:e1000428.
594 12. Chatterjee A, Johnson MA, Serrano P, Pedrini B, Joseph JS, Neuman BW, Saikatendu K,
595 Buchmeier MJ, Kuhn P, Wuthrich K. 2009. Nuclear magnetic resonance structure shows
596 that the severe acute respiratory syndrome coronavirus-unique domain contains a
597 macrodomain fold. J Virol 83:1823-36.

598 13. Makrynitsa GI, Ntonti D, Marousis KD, Birkou M, Matsoukas MT, Asami S, Bentrop D,
599 Papageorgiou N, Canard B, Coutard B, Spyroulias GA. 2019. Conformational plasticity
600 of the VEEV macro domain is important for binding of ADP-ribose. J Struct Biol
601 206:119-127.
602 14. Malet H, Coutard B, Jamal S, Dutartre H, Papageorgiou N, Neuvonen M, Ahola T,
603 Forrester N, Gould EA, Lafitte D, Ferron F, Lescar J, Gorbalenya AE, de Lamballerie X,
604 Canard B. 2009. The crystal structures of Chikungunya and Venezuelan equine
605 encephalitis virus nsP3 macro domains define a conserved adenosine binding pocket. J
606 Virol 83:6534-45.
607 15. Rack JG, Perina D, Ahel I. 2016. Macrodomains: Structure, Function, Evolution, and
608 Catalytic Activities. Annu Rev Biochem 85:431-54.
609 16. Li C, Debing Y, Jankevicius G, Neyts J, Ahel I, Coutard B, Canard B. 2016. Viral Macro
610 Domains Reverse Protein ADP-Ribosylation. J Virol 90:8478-86.
611 17. Eckei L, Krieg S, Butepage M, Lehmann A, Gross A, Lippok B, Grimm AR, Kummerer
612 BM, Rossetti G, Luscher B, Verheugd P. 2017. The conserved macrodomains of the non-
613 structural proteins of Chikungunya virus and other pathogenic positive strand RNA
614 viruses function as mono-ADP-ribosylhydrolases. Sci Rep 7:41746.
615 18. Fehr AR, Channappanavar R, Jankevicius G, Fett C, Zhao J, Athmer J, Meyerholz DK,
616 Ahel I, Perlman S. 2016. The Conserved Coronavirus Macrodomain Promotes Virulence
617 and Suppresses the Innate Immune Response during Severe Acute Respiratory Syndrome
618 Coronavirus Infection. mBio 7:e01721-16.
619 19. Kim DS, Challa S, Jones A, Kraus WL. 2020. PARPs and ADP-ribosylation in RNA
620 biology: from RNA expression and processing to protein translation and proteostasis.
621 Genes Dev 34:302-320.
622 20. Fehr AR, Singh SA, Kerr CM, Mukai S, Higashi H, Aikawa M. 2020. The impact of
623 PARPs and ADP-ribosylation on inflammation and host-pathogen interactions. Genes
624 Dev 34:341-359.
625 21. Eriksson KK, Cervantes-Barragan L, Ludewig B, Thiel V. 2008. Mouse hepatitis virus
626 liver pathology is dependent on ADP-ribose-1"-phosphatase, a viral function conserved in
627 the alpha-like supergroup. J Virol 82:12325-34.
628 22. Fehr AR, Athmer J, Channappanavar R, Phillips JM, Meyerholz DK, Perlman S. 2015.
629 The nsp3 macrodomain promotes virulence in mice with coronavirus-induced
630 encephalitis. J Virol 89:1523-36.
631 23. Grunewald ME, Chen Y, Kuny C, Maejima T, Lease R, Ferraris D, Aikawa M, Sullivan
632 CS, Perlman S, Fehr AR. 2019. The coronavirus macrodomain is required to prevent
633 PARP-mediated inhibition of virus replication and enhancement of IFN expression. PLoS
634 Pathog 15:e1007756.
635 24. Alhammad YMO, Fehr AR. 2020. The Viral Macrodomain Counters Host Antiviral
636 ADP-Ribosylation. Viruses 12:384.
637 25. Abraham R, Hauer D, McPherson RL, Utt A, Kirby IT, Cohen MS, Merits A, Leung
638 AKL, Griffin DE. 2018. ADP-ribosyl-binding and hydrolase activities of the alphavirus
639 nsP3 macrodomain are critical for initiation of virus replication. Proc Natl Acad Sci U S
640 A 115:E10457-E10466.
641 26. Abraham R, McPherson RL, Dasovich M, Badiee M, Leung AKL, Griffin DE. 2020.
642 Both ADP-Ribosyl-Binding and Hydrolase Activities of the Alphavirus nsP3
643 Macrodomain Affect Neurovirulence in Mice. mBio 11.

644 27. McPherson RL, Abraham R, Sreekumar E, Ong SE, Cheng SJ, Baxter VK, Kistemaker
645 HA, Filippov DV, Griffin DE, Leung AK. 2017. ADP-ribosylhydrolase activity of
646 Chikungunya virus macrodomain is critical for virus replication and virulence. Proc Natl
647 Acad Sci U S A 114:1666-1671.
648 28. Parvez MK. 2015. The hepatitis E virus ORF1 'X-domain' residues form a putative
649 macrodomain protein/Appr-1"-pase catalytic-site, critical for viral RNA replication. Gene
650 566:47-53.
651 29. Vuksanovic N, Silvaggi, N.R. National Science Foundation (NSF, United States). 2020.
652 High-resolution structure of the SARS-CoV-2 NSP3 Macro X domain doi:
653 10.2210/pdb6WEY/pdb. doi:10.2210/pdb6WEY/pdb.
654 30. Michalska K, Stols, L., Jedrzejczak, R., Endres, M., Babnigg, G., Kim, Y., Joachimiak,
655 A., Center for Structural Genomics of Infectious Diseases (CSGID). 2020. Crystal
656 Structure of ADP ribose phosphatase of NSP3 from SARS-CoV-2 in the apo doi:
657 10.2210/pdb6WEN/pdb. doi:10.2210/pdb6wen/pdb.
658 31. Michalska K, Kim, Y., Jedrzejczak, R., Maltseva, N., Endres, M., Mececar, A.,
659 Joachimiak, A., Center for Structural Genomics of Infectious Diseases (CSGID). 2020.
660 Crystal Structure of ADP ribose phosphatase of NSP3 from SARS CoV-2 in the complex
661 with ADP ribose doi: 10.2210/pdb6W02/pdb. doi:10.2210/pdb6W02/pdb.
662 32. Frick DN, Virdi RS, Vuksanovic N, Dahal N, Silvaggi NR. 2020. Molecular Basis for
663 ADP-Ribose Binding to the Mac1 Domain of SARS-CoV-2 nsp3. Biochemistry (Mosc)
664 59:2608-2615.
665 33. Jankevicius G, Hassler M, Golia B, Rybin V, Zacharias M, Timinszky G, Ladurner AG.
666 2013. A family of macrodomain proteins reverses cellular mono-ADP-ribosylation. Nat
667 Struct Mol Biol 20:508-14.
668 34. Leung AKL, McPherson RL, Griffin DE. 2018. Macrodomain ADP-ribosylhydrolase and
669 the pathogenesis of infectious diseases. PLoS Pathog 14:e1006864.
670 35. Lei J, Kusov Y, Hilgenfeld R. 2018. Nsp3 of coronaviruses: Structures and functions of a
671 large multi-domain protein. Antiviral Res 149:58-74.
672 36. Heer CD, Sanderson DJ, Alhammad YMO, Schmidt MS, Trammell SAJ, Perlman S,
673 Cohen MS, Fehr AR, Brenner C. 2020. Coronavirus and PARP expression dysregulate
674 the NAD Metabolome: a potentially actionable component of innate immunity. bioRxiv
675 doi:10.1101/2020.04.17.047480.
676 37. Shull NP, Spinelli SL, Phizicky EM. 2005. A highly specific phosphatase that acts on
677 ADP-ribose 1"-phosphate, a metabolite of tRNA splicing in Saccharomyces cerevisiae.
678 Nucleic Acids Res 33:650-60.
679 38. Rosenthal F, Feijs KL, Frugier E, Bonalli M, Forst AH, Imhof R, Winkler HC, Fischer D,
680 Caflisch A, Hassa PO, Luscher B, Hottiger MO. 2013. Macrodomain-containing proteins
681 are new mono-ADP-ribosylhydrolases. Nat Struct Mol Biol 20:502-7.
682 39. Sharifi R, Morra R, Appel CD, Tallis M, Chioza B, Jankevicius G, Simpson MA, Matic I,
683 Ozkan E, Golia B, Schellenberg MJ, Weston R, Williams JG, Rossi MN, Galehdari H,
684 Krahn J, Wan A, Trembath RC, Crosby AH, Ahel D, Hay R, Ladurner AG, Timinszky G,
685 Williams RS, Ahel I. 2013. Deficiency of terminal ADP-ribose protein glycohydrolase
686 TARG1/C6orf130 in neurodegenerative disease. EMBO J 32:1225-37.
687 40. Gibson BA, Conrad LB, Huang D, Kraus WL. 2017. Generation and Characterization of
688 Recombinant Antibody-like ADP-Ribose Binding Proteins. Biochemistry (Mosc)
689 56:6305-6316.

41. Affar EB, Duriez PJ, Shah RG, Winstall E, Germain M, Boucher C, Bourassa S, Kirkland JB, Poirier GG. 1999. Immunological determination and size characterization of poly(ADP-ribose) synthesized in vitro and in vivo. Biochim Biophys Acta 1428:137-46.
42. Asokanathan C, Tierney S, Ball CR, Buckle G, Day A, Tanley S, Bristow A, Markey K, Xing D, Yuen CT. 2018. An ELISA method to estimate the mono ADP-ribosyltransferase activities: e.g in pertussis toxin and vaccines. Anal Biochem 540-541:15-19.
43. Langelier MF, Planck JL, Servent KM, Pascal JM. 2011. Purification of human PARP-1 and PARP-1 domains from Escherichia coli for structural and biochemical analysis. Methods Mol Biol 780:209-26.
44. Wang Z, Gagne JP, Poirier GG, Xu W. 2014. Crystallographic and biochemical analysis of the mouse poly(ADP-ribose) glycohydrolase. PLoS One 9:e86010.
45. Kabsch W. 1988. Evaluation of Single-Crystal X-Ray-Diffraction Data from a Position-Sensitive Detector. J Appl Crystallogr 21:916-924.
46. Kabsch W. 2010. Xds. Acta Crystallogr D Biol Crystallogr 66:125-32.
47. Vonrhein C, Flensburg C, Keller P, Sharff A, Smart O, Paciorek W, Womack T, Bricogne G. 2011. Data processing and analysis with the autoPROC toolbox. Acta Crystallogr D Biol Crystallogr 67:293-302.
48. Evans PR. 2011. An introduction to data reduction: space-group determination, scaling and intensity statistics. Acta Crystallogr D Biol Crystallogr 67:282-92.
49. McCoy AJ, Grosse-Kunstleve RW, Adams PD, Winn MD, Storoni LC, Read RJ. 2007. Phaser crystallographic software. J Appl Crystallogr 40:658-674.
50. Adams PD, Afonine PV, Bunkoczi G, Chen VB, Davis IW, Echols N, Headd JJ, Hung LW, Kapral GJ, Grosse-Kunstleve RW, McCoy AJ, Moriarty NW, Oeffner R, Read RJ, Richardson DC, Richardson JS, Terwilliger TC, Zwart PH. 2010. PHENIX: a comprehensive Python-based system for macromolecular structure solution. Acta Crystallogr D Biol Crystallogr 66:213-21.
51. Emsley P, Lohkamp B, Scott WG, Cowtan K. 2010. Features and development of Coot. Acta Crystallogr D Biol Crystallogr 66:486-501.
52. Chen VB, Arendall WB, 3rd, Headd JJ, Keedy DA, Immormino RM, Kapral GJ, Murray LW, Richardson JS, Richardson DC. 2010. MolProbity: all-atom structure validation for macromolecular crystallography. Acta Crystallogr D Biol Crystallogr 66:12-21.
53. Potterton L, McNicholas S, Krissinel E, Gruber J, Cowtan K, Emsley P, Murshudov GN, Cohen S, Perrakis A, Noble M. 2004. Developments in the CCP4 molecular-graphics project. Acta Crystallogr D Biol Crystallogr 60:2288-94.
54. Krissinel E. 2012. Enhanced fold recognition using efficient short fragment clustering. J Mol Biochem 1:76-85.
55. Evans P. 2006. Scaling and assessment of data quality. Acta Crystallogr D Biol Crystallogr 62:72-82.
56. Diederichs K, Karplus PA. 1997. Improved R-factors for diffraction data analysis in macromolecular crystallography. Nat Struct Biol 4:269-75.
57. Weiss MS. 2001. Global indicators of X-ray data quality. J Appl Crystallogr 34:130-135.
58. Evans P. 2012. Resolving some old problems in protein crystallography. Science 336:986-7.
59. Karplus PA, Diederichs K. 2012. Linking crystallographic model and data quality. Science 336:1030-3.

736
737 **FIGURE LEGENDS**

738 **Figure 1.** The SARS-CoV-2 Mac1 is a small domain within nsp3 and is highly conserved
739 between other human CoV Mac1 protein domains. (A) Cartoon Schematic of the SARS-CoV-2
740 non-structural protein 3. The conserved macrodomain, or Mac1, is highlighted in yellow. (B)
741 Sequence alignment of Mac1 from CoVs; SARS-CoV-2, SARS-CoV, MERS-CoV, and mouse
742 hepatitis virus (MHV), and from alphaviruses Venezuelan equine encephalitis virus (VEEV) and
743 sindbis virus (SINV), and hepatitis E virus (HEV). Sequences were aligned using the ClustalW
744 method from Clustal Omega online tool with manual adjustment. Identical residues are bolded,
745 shaded in grey, and marked with asterisks; semiconserved residues were shaded in grey and
746 marked with two dots (one change amongst all viruses) or one dot (2 changes or conserved
747 within CoV family).

748 **Figure 2.** Structure of SARS-CoV-2 Mac1 complexed with ADP-ribose. **A)** The structure was
749 rendered as a blend through model from the N-terminus (blue) to the C-terminus (red). **B)** The
750 structure was colored by secondary structure showing sheets (magenta) and helices (green). The
751 ADP-ribose is rendered as gray cylinders with oxygens and nitrogens colored red and blue,
752 respectively.

753 **Figure 3.** Binding mode of ADP-ribose in SARS-CoV-2 Mac1. **A)** Fo-Fc Polder omit map
754 (green mesh) contoured at 3σ. **B)** Hydrogen bond interactions (dashed lines) between ADP-
755 ribose and amino acids. **C)** Interactions with water molecules. Direct hydrogen bond interactions
756 are represented by dashed lines and water mediated contacts to amino acids are drawn as solid
757 lines.

758 **Figure 4**. Structural comparison of the SARS-CoV-2 Mac1 protein with the SARS-CoV and
759 MERS-CoV Mac1 proteins. **A-B)** Superposition of SARS-CoV-2 macrodomain (magenta) with

760 coronavirus macrodomain structures. **A**) SARS-CoV Mac1 with ADP-ribose (gold) (2FAV) and
761 **B**) MERS-CoV Mac1 with ADP-ribose (teal) (5HOL). **C-D)** Superposition of SARS-CoV-2
762 Mac1 (magenta) with other coronavirus Mac1 structures highlighting the ADP-ribose binding
763 site. **C**) SARS-CoV (gold), **D**) MERS-CoV (teal). The ADP-ribose molecules are colored gray
764 for SARS-CoV-2 Mac1 (**A-D**) and are rendered as green cylinders for SARS-CoV Mac1 (panel
765 **A,C**) and MERS-CoV Mac1 (panel **B,D**).
766 **Figure 5**. Human CoVs bind to ADP-ribose with similar affinity. **A-B)** ADP-ribose binding of
767 human Mdo2 and SARS-CoV, MERS-CoV, and SARS-CoV-2 Mac1 proteins by ITC. Images in
768 **(A)** are of one experiment representative of at least 2 independent experiments. Data in **(B)**
769 represent the combined averages of multiple independent experiments for each protein. Mdo2
770 n=2; SARS-CoV n=5; MERS-CoV n=6; SARS-CoV-2 n=2.
771 **Figure 6**. Coronavirus Mac1 proteins are ADP-ribosylhydrolases. **A)** The SARS-CoV-2
772 macrodomain was incubated with MARylated PARP10 CD *in vitro* at equimolar ratios (1 μM)
773 for the indicated times at 37°C. ADP-ribosylated PARP10 CD was detected by immunoblot (IB)
774 with anti-ADP-ribose binding reagent (Millipore-Sigma MAB1076). Total PARP10 CD and
775 macrodomain protein levels were determined by Coomassie Blue (CB) staining. PARP10 CD
776 incubated alone at 37°C was stopped at 0 or 60 minutes. **B)** The level of de-MARylation was
777 measured by quantifying band intensity using Image J software. Intensity values were plotted
778 and fit to a non-linear regression curve with error bars representing standard deviation. Results in
779 **A** are representative experiments of two independent experiments and data in **B** represent the
780 combined results of the two independent experiments. **C)** The Mdo2, MERS-CoV, SARS-CoV,
781 and SARS-CoV-2 macrodomains were incubated with MARylated PARP10 CD *in vitro* at the
782 following ratios of [substrate]:[Mac1]: 1:1 (1 μM), 5:1 (500 nM, 100 nM), or 10:1 (1 μM, 100

783 nM) for the indicated times at 37°C. ADP-ribosylated PARP10 CD was detected as described
784 above, and total PARP10 CD and macrodomain protein levels were determine by Coomassie
785 Blue (Fig. S6). **D)** Time-dependent substrate concentrations were determined by quantifying
786 band intensity using Image Studio software. The data were then analyzed using Mathematica 12,
787 as described in Methods, to determine the initial rate (*k*) of substrate decay. Results in **C** are
788 representative experiments of three independent experiments and data in **D** represent the
789 combined results of the three independent experiments.
790 **Fig. 7.** Coronavirus Mac1 proteins do not hydrolyze PAR. PAR hydrolase assays were performed
791 with PARP1 either extensively poly-ADP-ribosylated (500 μM NAD^+) or partially poly-ADP-
792 ribosylated (5 μM NAD^+) to produce oligo-ADP-ribose. Macrodomains were incubated with
793 both automodified PARP1 substrates for 1 hour. PAR was detected by immunoblot with the anti-
794 PAR antibody 96-10. PARG (catalytically active 60 kD fragment) was used as a positive control.
795 The results are representative of 2 independent experiments.
796 **Figure 8.** Development of an ELISA assay to detect de-MARylation. **A)** Cartoon schematic of
797 the ELISA assay. ELISA plates pre-coated with glutathione and pre-blocked were used capture
798 GST-tagged PARP10 proteins, which was used as a substrate for de-MARylation. The removal
799 of MAR was detected by anti-MAR antibodies. **B)** MARylated PARP10 (MAR+) and non-
800 MARylated PARP10 (MAR-) with no SARS-CoV-2 Mac1 as controls were detected with anti-
801 mono-ADP-ribose binding reagent (α-MAR) (Millipore-Sigma MAB1076) or with anti-GST (α-
802 GST) (Invitrogen, MA4-004). **C)** Starting at 12.5 nM, 2-fold serial dilutions of the SARS-CoV-2
803 Mac1 protein was incubated in individual wells with MARylated PARP10-CD for 60 min at
804 37°C**.** The graph represents the combined results of 2 independent experiments.
805

SUPPLEMENTAL FIGURE LEGENDS

Figure S1. Purification and crystallization of macrodomain proteins. **A)** Macrodomain proteins were purified as described in Methods. Equimolar amounts of the recombinant proteins were run on a polyacrylamide gel and visualized by Coomassie staining. **B)** Crystals of SARS-CoV-2 Mac1 obtained with Salt Rx HT E10 supplemented with 0.1 M NDSB-256.

Figure S2. Extended residues at the C-terminus of the SARS-CoV-2 Mac1 clashed with symmetry related molecules. **A)** Comparison of the amino acid sequence of SARS-CoV-2 Mac1, 6W02 and 6WEY. **B)** Superposition of SARS-CoV-2 Mac1 (magenta) subunit B onto subunit A of 6W02 reveals that the C-terminus would clash with symmetry related molecules (coral).

Figure S3. Comparison of the SARS-CoV-2 Mac1 protein with homologous structures. **A-B)** Superposition of SARS-CoV-2 Mac1 (magenta) with other recently determined homologous structures. **A)** SARS-CoV-2 Mac1 apo structure (6WEN), **B)** SARS-CoV-2 Mac1 complexed with ADP-ribose (6W02). The ADP-ribose molecule is colored gray for SARS-CoV-2 and is represented as green cylinders for 6W02 in panel **B**. **C-D)** Comparison of the residues in the ADP-ribose binding site. **C**) SARS-CoV-2 Mac1 apo structure (blue, 6WEN), **D**) SARS-CoV-2 Mac1 complexed with ADP-ribose (green, 6W02). The ADP-ribose of SARS-CoV-2 is rendered as gray cylinders, and is represented as green cylinders for 6W02 in panel **B**.

Figure S4. ADP-ribose binding of macrodomain proteins by DSF assay. The macrodomain proteins (10 μM) were incubated with increasing concentrations of ADP-ribose and measured by DSF as described in Methods. Mdo2 n=4; SARS-CoV n=6; MERS-CoV n=5; SARS-CoV-2 n=3.

Figure S5. Affinity of ADP-ribose binding antibodies for ADP-ribosylated PARP10 CD. MARylated PARP10 and non-MARylated PARP10 CD were detected by immunoblot (IB) with anti-GST (Invitrogen, MA4-004), anti-ADP-ribose binding reagents: anti-MAR (Millipore-

829 Sigma MAB1076), anti-PAR (Millipore-Sigma MABC547), and anti-MAR/PAR (Millipore-
830 Sigma MABE1075) antibodies.

831 **Figure S6.** MARylated PARP10 stability over time. The presence of mono-ADP-ribose of
832 automodified PARP10 without any macrodomain was detected at 6 time points by immunoblot
833 analysis with the anti-GST (Invitrogen, MA4-004) and anti-ADP-ribose binding reagent anti-
834 MAR (Millipore-Sigma MAB1076).

835 **Figure S7.** The CoVs and human Mdo2 macrodomain proteins were incubated with MARylated
836 PARP10 CD *in vitro* for the indicated times at 37°C. Total PARP10 CD and macrodomain
837 protein levels were determined by Coomassie Blue (CB) staining. Results showone experiment
838 of three independent experiments.

839 **Figure S8**. Differential PARylation of PARP1 by varying concentrations of NAD^+. Recombinant
840 human PARP1 was automodified in a reaction buffer supplemented with increasing
841 concentrations of NAD^+ to generate substrates for the PAR hydrolase assays. PAR was detected
842 by immunoblot analysis of reaction products with the anti-PAR antibody 96-10.

A

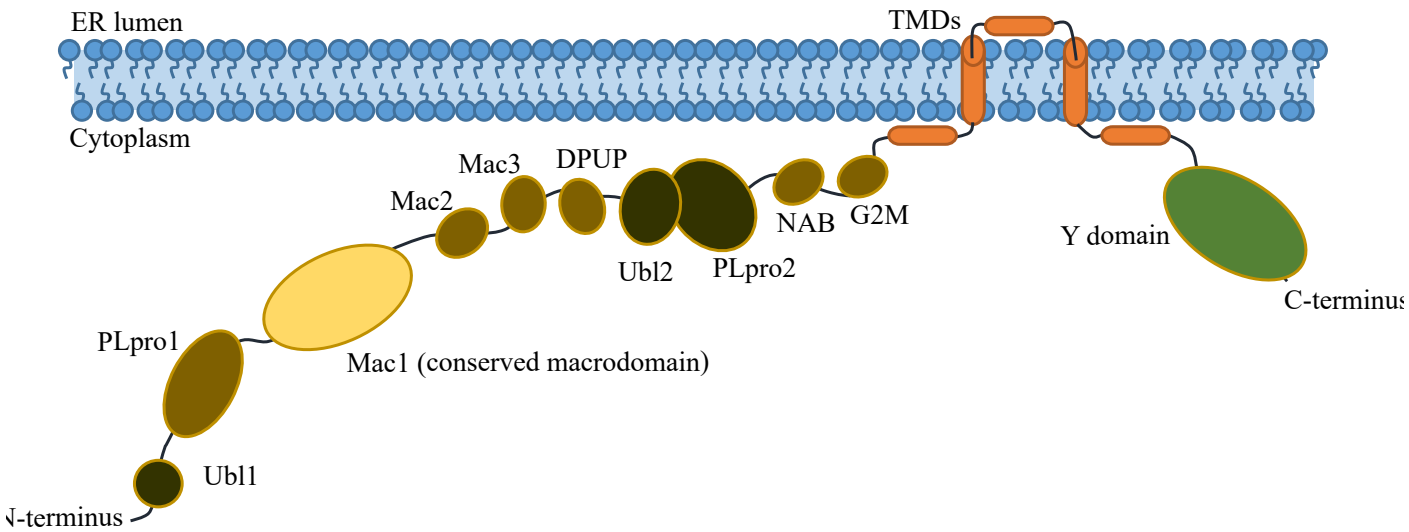

B

```
SARS-CoV-2 aa          10        20        30        40        50        60        70
                       |         |         |         |         |         |         |
SARS-CoV-2    IEVNSFSGYLKLT-----DNVYIKNADIVEEAKKVKPTVVVNAANVYLKHGGGVAGALNKATNNAMQVESDDYIATNGP  74
SARS-CoV      EPVNQFTGYLKLT-----DNVAIKCVDIVKEAQSANPMVIVNAANIHLKHGGGVAGALNKATNGAMQKESDDYIKLNGP  74
MERS-CoV      -PLSNFEH-KVIT-----ECVTIVLGDAIQVAKCYGESVLVNAANTHLKHGGGIAGAINAASKGAVQKESDEYILAKGP  72
MHV           -----LYG-SCIT-----PNVCFVKGDVIKVLRRVGAEVIVNPANGRMAHGAGVAGAIAKAAGKAFINETADMVKAQGV  68
VEEV          -----YTG-SRLHEAGCAPSYHVVRGDI----ATATEGVIINAANSKGQPGGGVCGALYKKFPESFDLQPIE-------  62
SINV          ----------------APSYRTKRENI----ADCQEEAVVNAANPLGRPGEGVCRAIYKRWPNSFTDSATE-------  51
HEV           ----------------YPDGSKVFAGSL----FESTCTWLVNASNVDHRPGGGLCHAFYQRYPASFDAASFVMR-----  54
Conservation                .         .         .          . :*::*     * * ..        .    .

SARS-CoV-2 a.a.   80        90        100       110       120       130       140
                  |         |         |         |         |         |         |
SARS-CoV-2    LKVGGSCVLSGHNLAKHCLHVVGPNVNK--G-EDIQLLKSAYEVF------NQHEVLLAPLLSAGIFGADPIH---SLR  141
SARS-CoV      LTVGGSCLLSGHNLAKKCLHVVGPNLNA--G-EDIQLLKAAYENF------NSQDILLAPLLSAGIFGAKPLQ---SLQ  141
MERS-CoV      LQVGDSVLLQGHSLAKNILHVVGPDARA--K-QDVSLLSKCYKAM------NAYPLVVTPLVSAGIFGVKPAV---SFD  139
MHV           CQVGGCYESTGGKLCKKVLNIVGPDARGHGK-QCYSLLERAYQHI------NKCDNVVTTLISAGIFSVPTDV---SLT  137
VEEV          --VGKARLVK--GVTKHIIHAVGPNFNKVSEVEGDKQLAEAYESIAKIVNDNNYKSVAIPLLSTGIFSGNKDRLTQSLN  137
SINV          --TGTAKLTV--CQGKKVIHAVGPDFRKHPEAEALKLLQNAYHAVADLVNEHNIKSVAIPLLSTGIYAAGKDRLEVSLN  126
HEV           --DGAAAY---TLTPRPIIHAVAPDYRL--E-HNPKRLEAAYRETC-----SRLGTAAYPLLGTGIYQVPIGP---SFD  117
Conservation    .*          .  .: *:*         .*  :*       .      :* :.**.        *.

SARS-CoV-2 a.a.       150       160
                      |         |
SARS-CoV-2    VC---VDTVRTNVYLAVFDKNLYDKLV---------------- 165
SARS-CoV      VC---VQTVRTQVYIAVNDKALYEQVVMDYLDNL--------- 172
MERS-CoV      YL---IREAKTRVLVVVNSQDVYKSLTIVDIPQLE-------- 171
MHV           YL---LGVVTKNVILVSNNQDDFDVIEKCQVTSVAGTK----- 172
VEEV          HLLTALDTTDADVAIYCRDKKWEMT------------------ 162
SINV          CLTTALDRTDADVTIYCLDKKWKERI--DAVLQLKE------- 160
HEV           AWER-NHRPGDELYLPELAARWFEANRPTRPTLIITEDVARTA 159
Conservation              :
```

A

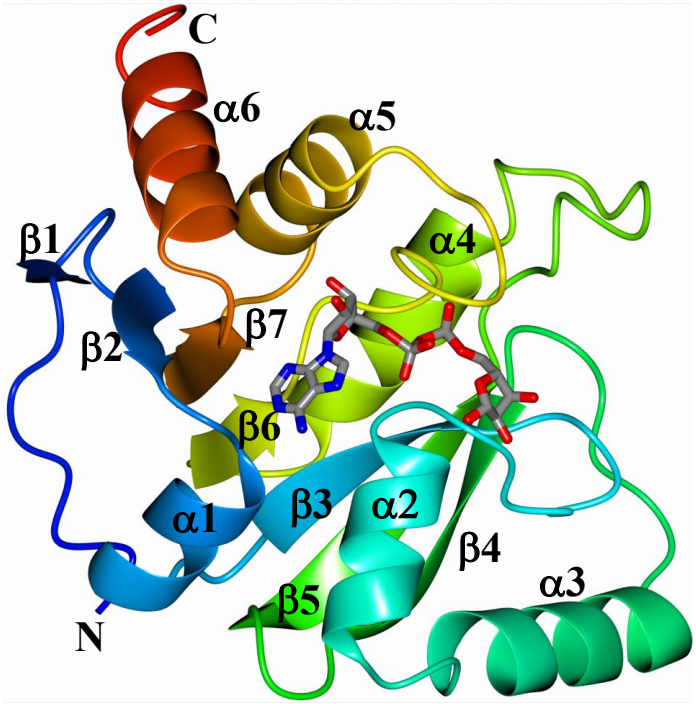

β1: L10-K11
β2: V16-A21
α1: I23-V30
β3: V34-A39
α2: V49-T57
α3: A60-N72
β4: S79-G85
β5: A89-V96
α4: L108-Q118
β6: V121-A124
α5: P136-T146
β7: N150-V155
α6: K158-F168

B

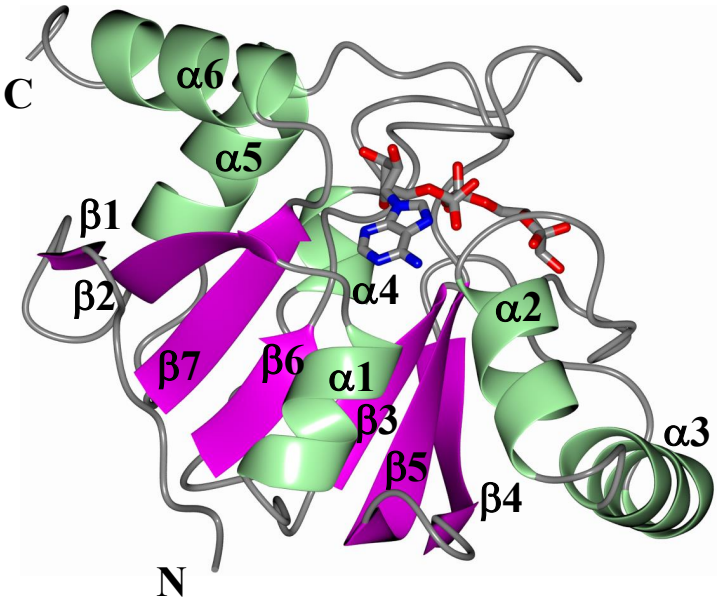

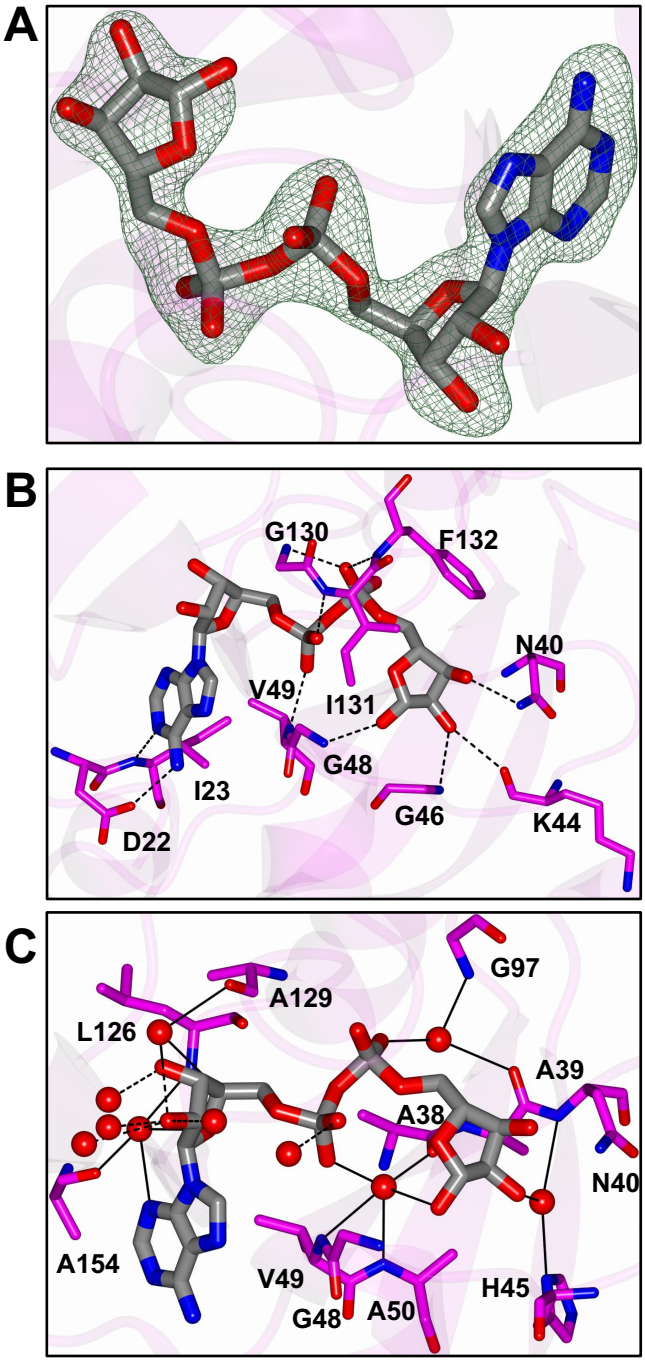
A
B
G130
F132
N40
V49
I131
G48
I23
G46
K44
D22
C
G97
A129
L126
A39
A38
N40
A154
V49
H45
G48
A50

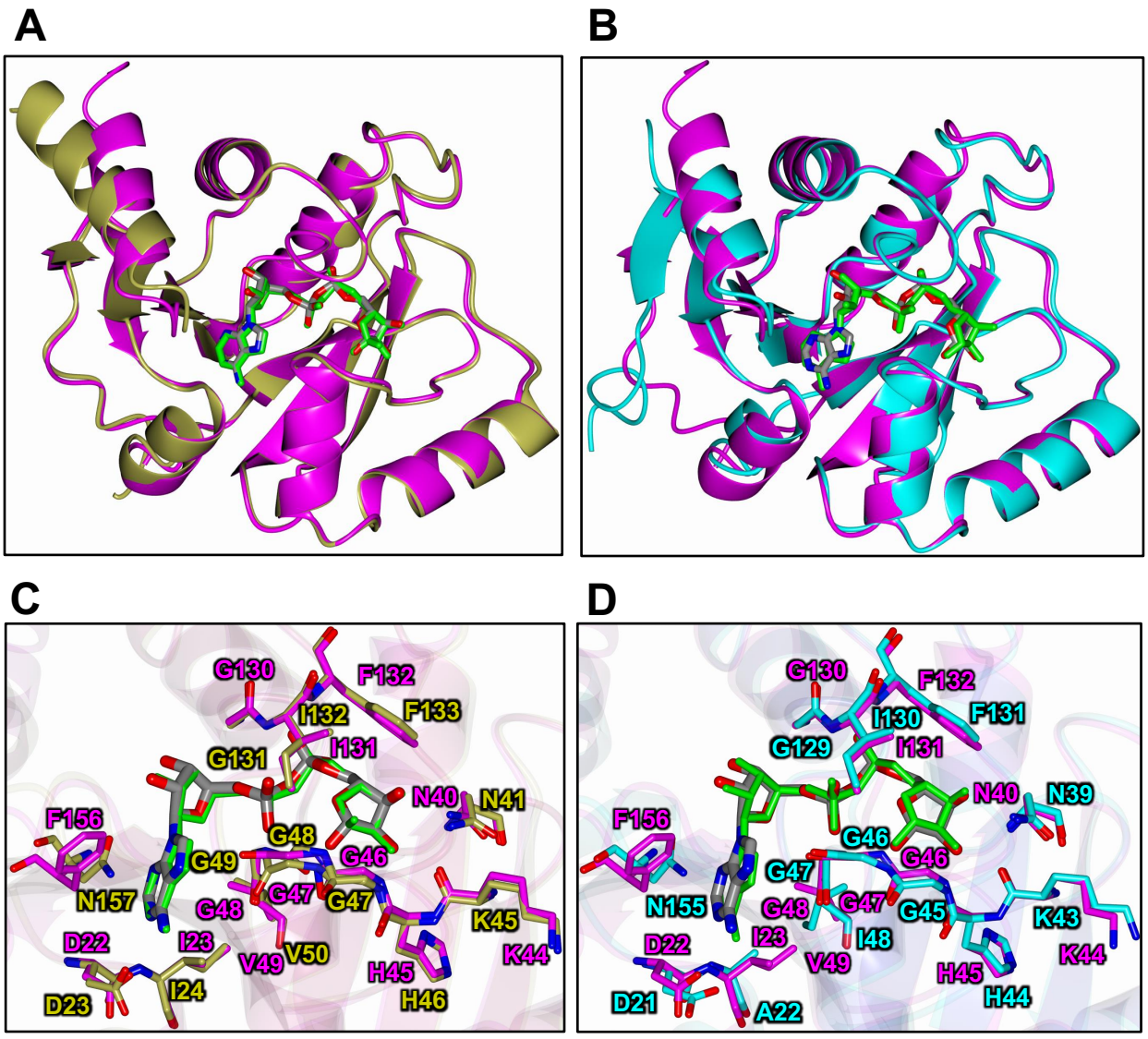
A
B
C
G130
F132
I132
F133
I131
G131
N40
N41
F156
G48
G49
G46
N157
G47
G47
G48
K45
D22
I23
V49
V50
K44
H45
I24
H46
D23
D
G130
F132
I130
F131
G129
I131
N40
N39
F156
G46
G46
G47
N155
G48
G47
G45
K43
I23
I48
D22
V49
K44
H45
H44
D21
A22

A

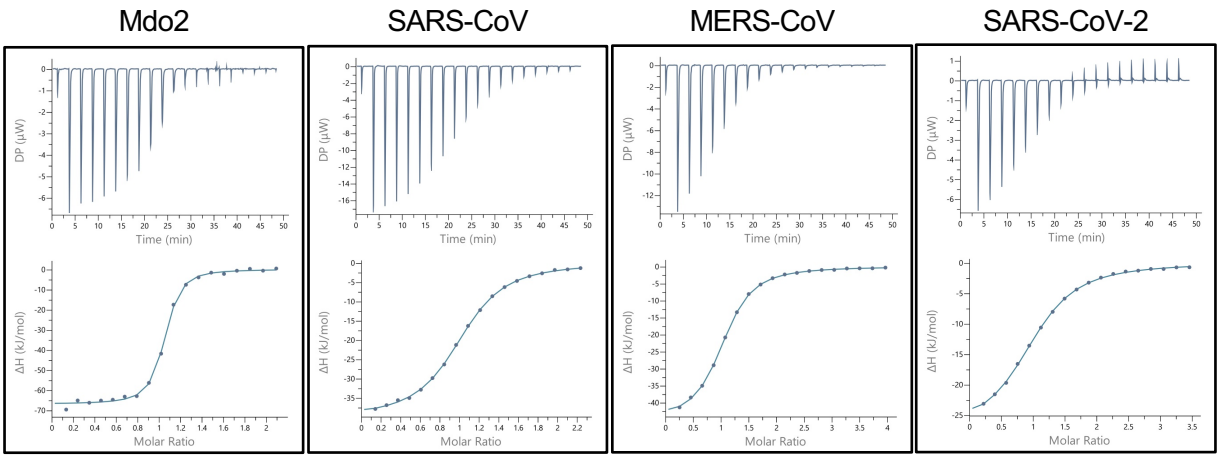

B

Macrodomain	Stoichiometry (N)	Kd (µM)	ΔH (kcal/mol)	ΔG (kcal/mol)
Mdo2	0.92 ± 0.01	0.24 ± 0.02	-66 ± 1	-38 ± 2
SARS-CoV	0.89 ± 0.04	10.8 ± 1.7	-40 ± 1.2	-28 ± 0.4
MERS-CoV	0.97 ± 0.04	7.9 ± 0.15	-47 ± 3	-29 ± 0.4
SARS-CoV-2	1.14 ± 0.06	16.8 ± 0.04	-28 ± 0.1	-27 ± 0.1

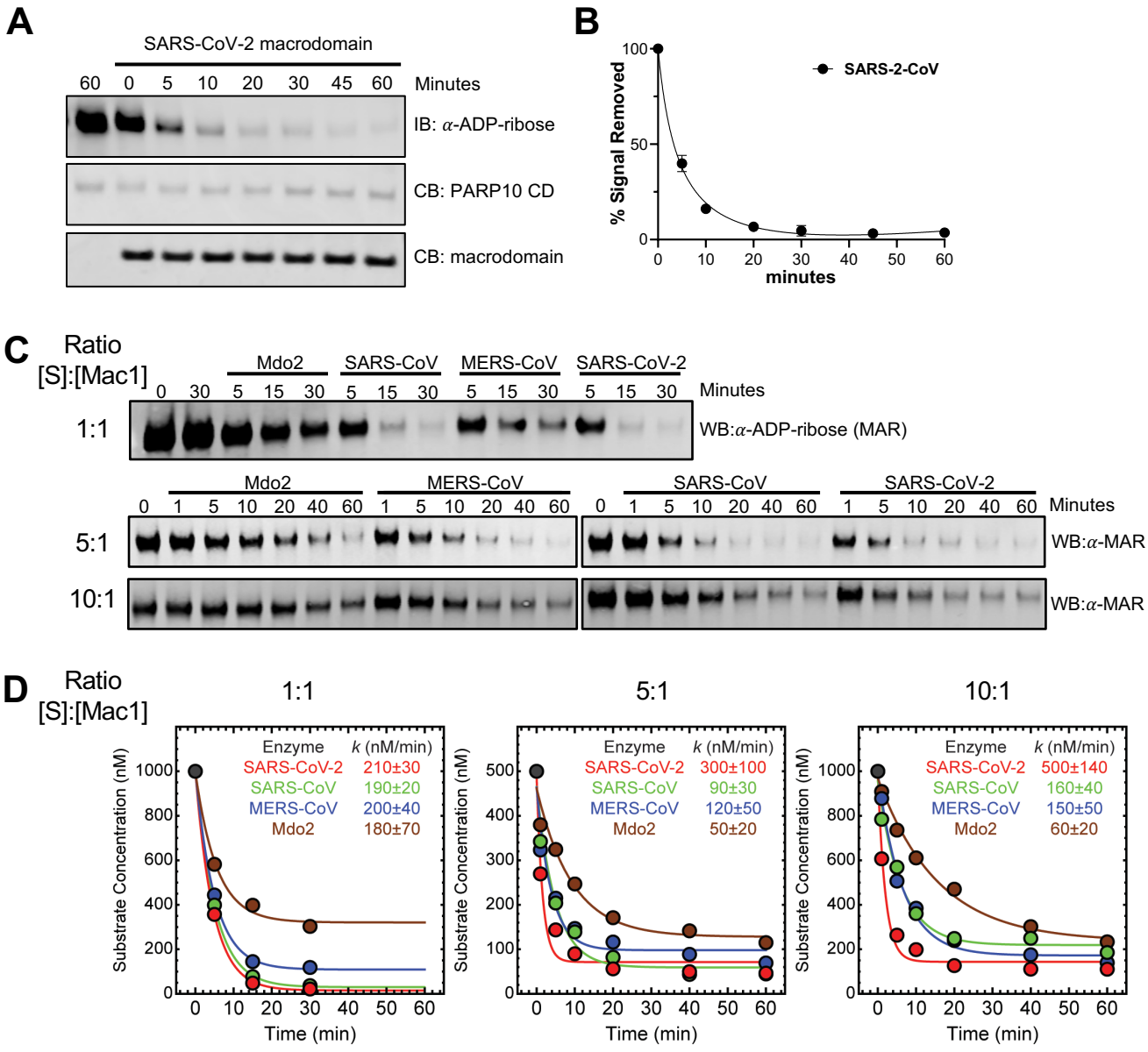
A
SARS-CoV-2 macrodomain
60 0 5 10 20 30 45 60 Minutes
IB: α-ADP-ribose
CB: PARP10 CD
CB: macrodomain
B
SARS-2-CoV
% Signal Removed
100
50
0
0 10 20 30 40 50 60
minutes
C
Ratio [S]:[Mac1]
Mdo2 SARS-CoV MERS-CoV SARS-CoV-2
0 30 5 15 30 5 15 30 5 15 30 5 15 30 Minutes
1:1
WB:α-ADP-ribose (MAR)
Mdo2 MERS-CoV SARS-CoV SARS-CoV-2
0 1 5 10 20 40 60 1 5 10 20 40 60 0 1 5 10 20 40 60 1 5 10 20 40 60 Minutes
5:1
WB:α-MAR
10:1
WB:α-MAR
D
Ratio [S]:[Mac1]
1:1
5:1
10:1
Enzyme k (nM/min)
SARS-CoV-2 210±30
SARS-CoV 190±20
MERS-CoV 200±40
Mdo2 180±70
Enzyme k (nM/min)
SARS-CoV-2 300±100
SARS-CoV 90±30
MERS-CoV 120±50
Mdo2 50±20
Enzyme k (nM/min)
SARS-CoV-2 500±140
SARS-CoV 160±40
MERS-CoV 150±50
Mdo2 60±20
Substrate Concentration (nM)
Time (min)

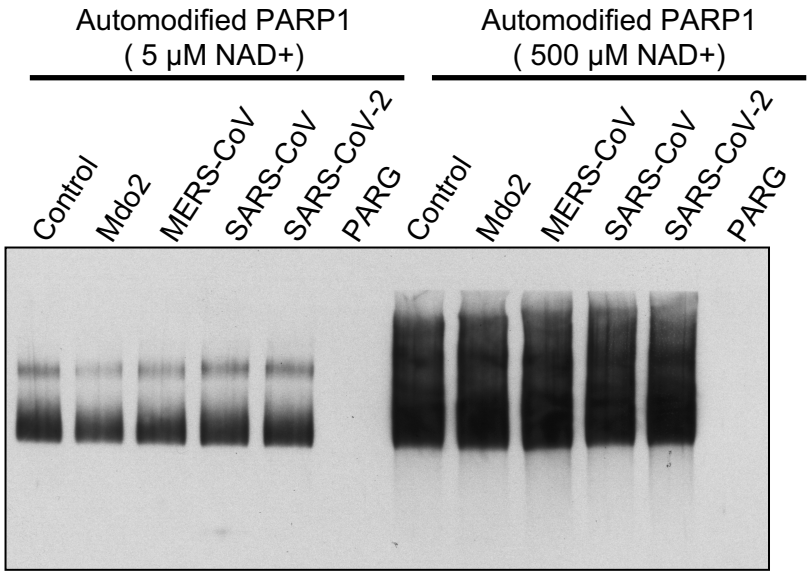
Automodified PARP1
(5 μM NAD+)
Automodified PARP1
(500 μM NAD+)
Control
Mdo2
MERS-CoV
SARS-CoV
SARS-CoV-2
PARG
Control
Mdo2
MERS-CoV
SARS-CoV
SARS-CoV-2
PARG

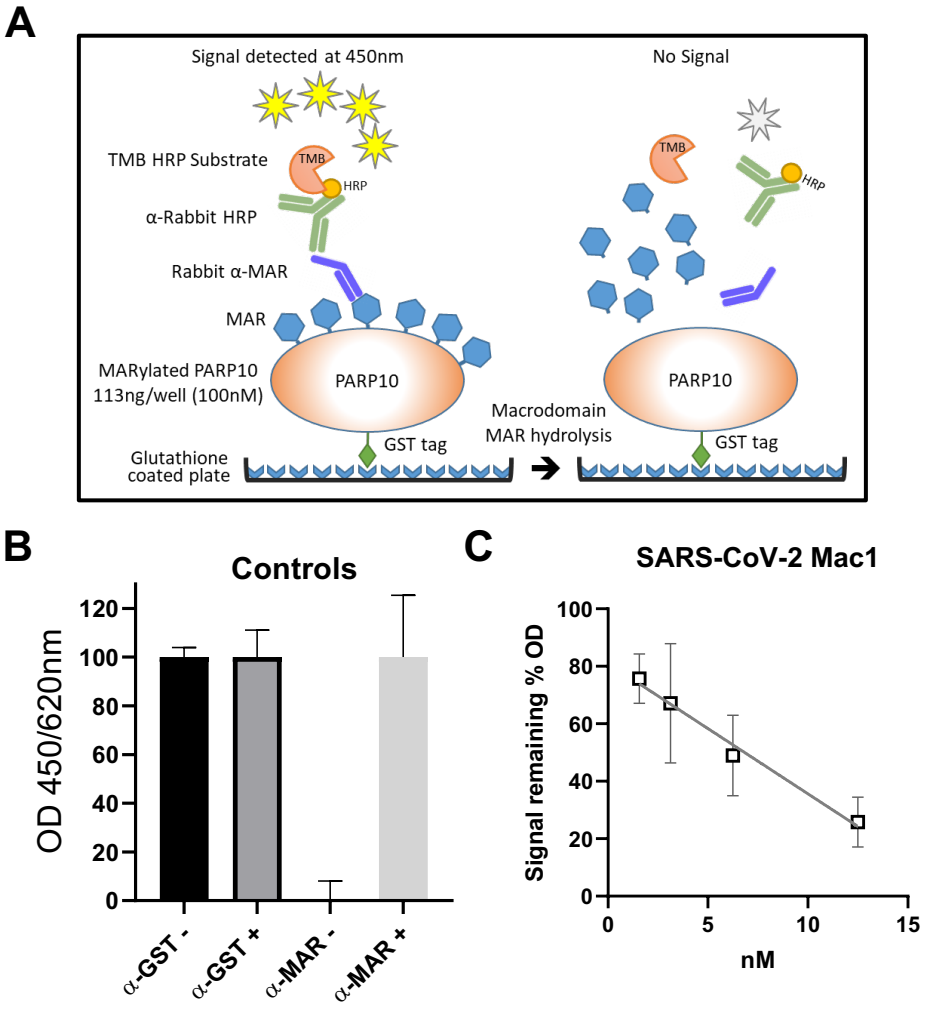
A
Signal detected at 450nm
No Signal
TMB HRP Substrate
TMB
HRP
α-Rabbit HRP
Rabbit α-MAR
MAR
MARylated PARP10
113ng/well (100nM)
PARP10
GST tag
Glutathione
coated plate
Macrodomain
MAR hydrolysis
B
Controls
OD 450/620nm
120
100
80
60
40
20
0
α-GST -
α-GST +
α-MAR -
α-MAR +
C
SARS-CoV-2 Mac1
Signal remaining % OD
100
80
60
40
20
0
0
5
10
15
nM